Dynamic Characteristics of VCSELs for Cs-Based MEMS Atomic Clocks

Ahmed Al-Samaneh and Dietmar Wahl

We have fabricated flip-chip-bondable vertical-cavity surface-emitting lasers (VCSELs) emitting at 894.6 nm wavelength for Cs-based atomic clock applications. For polarization control, we have integrated shallow semiconducting surface gratings in the top Bragg mirror. A modulation bandwidth of more than 5 GHz is reached at only 0.5 mA bias. Modulation current efficiency factors larger than 12 GHz/$\sqrt{mA}$ are achieved. The intrinsic modulation characteristics of the VCSELs are investigated by precisely fitting measured small-signal modulation response curves and relative intensity noise spectra. A K-factor of less than 0.40 ns and a maximum 3 dB bandwidth exceeding 22 GHz are obtained.

1. Introduction

There is much recent interest in atomic clocks with low power consumption, ultra-small volume, and long-term instabilities below, e.g., 10^{-11} over one day. Mobile satellite navigation and the synchronization of communication networks are most prominent applications. For example, miniaturized atomic clocks would be important elements for the precision time protocol (PTP), which is an approach to distribute synchronization over next-generation IP-based packet networks.

VCSELs are compelling light sources for such clocks, since they simultaneously meet the requirements of high-temperature operation while emitting a low-noise, narrow-linewidth, single-mode, single-polarization beam. Employing the coherent population trapping (CPT) effect [1] of the Cs D1 line, the laser is harmonically modulated at about 4.6 GHz with a center wavelength of about 894.6 nm. Sub-mA threshold currents of VCSELs contribute to low dissipated power, and the vertical emission is advantageous for hybrid integration with the clock microsystem. In addition to employing CPT, the realization of ultra-miniaturized atomic clocks requires fabrication techniques known from micro-electro-mechanical systems (MEMS). In 2008, the European Commission (EC) launched the collaborative research project *MEMS atomic clocks for timing, frequency control & communications* (MAC-TFC, www.mac-tfc.eu) within its seventh framework programme, aiming to realize the first European miniature-size atomic clock.

2. VCSEL Design and Fabrication

The VCSEL wafers are grown by solid-source molecular beam epitaxy on n-doped (100)-oriented GaAs substrates. The VCSEL layer structure is as described in [2]. For polarization control, we have integrated shallow semiconducting surface gratings in a quarter-wave

thick GaAs antiphase layer added to the top Bragg mirror [3]. Such an inverted grating has quarter-wave etch depth, 0.6 or 0.7 µm period, and 50 % duty cycle. As expected from the design, the polarization is orthogonal to the grating lines.

For the purpose of integration with the atomic clock microsystem, flip-chip-bondable VCSEL chips have been realized. As seen in Fig. 1 (left), the chip has a size of 300 × 300 µm^2 and can be RF- (radio frequency) tested on-wafer using microwave probes with a signal–ground configuration. However, the design involves increased processing complexity compared to regular VCSELs with a substrate-side n-contact. This originates from the necessity of etching mesas down to the highly n-doped contact layer, applying several polyimide planarizaion layers containing dicing trenches as well as circular holes for n-vias, and electroplating of Au n-vias. As the last step, bondpads are evaporated. Figure 1 (right) depicts a cross-sectional view of a flip-chip-bondable VCSEL chip.

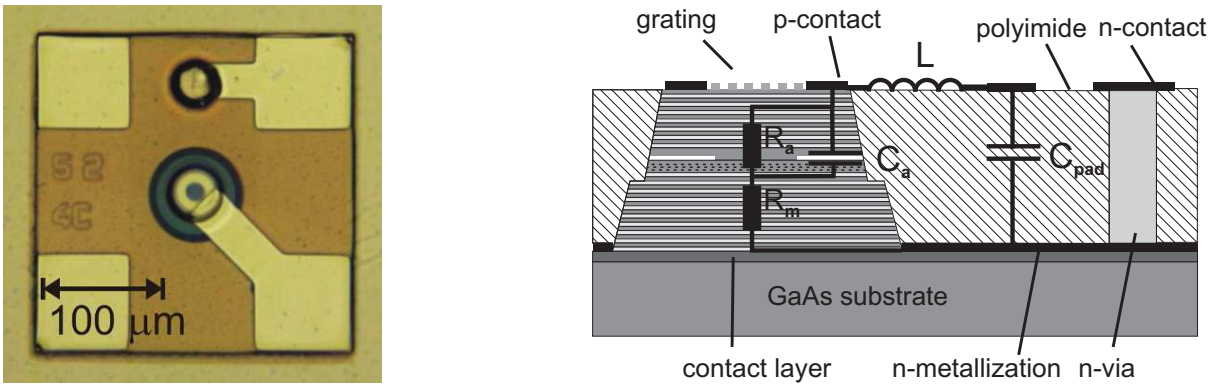

Fig. 1: Optical micrograph of a fully processed flip-chip-bondable VCSEL chip to be incorporated into atomic clock microsystems (left) and a schematic cross-sectional drawing with an associated equivalent-circuit model (right).

3. Dynamic Characterization

Cs-based MEMS atomic clocks require VCSELs with modulation bandwidths exceeding 5 GHz at low driving currents of, e.g., 2 mA. In this section, the dynamic characteristics of flip-chip-bondable VCSEL chips are presented; mainly the small-signal modulation response. The microwave reflection spectra of the VCSEL chips are also measured, as well as the relative intensity noise (RIN) spectra as a means to determine the intrinsic modulation behavior of the lasers.

3.1 Small-signal modulation characteristics

Small-signal modulation response curves of flip-chip-bondable VCSELs have been measured. In what follows, all modulation response functions relate the square of the fluctuations of the optical output power to those of the modulating electrical power. In other words, they relate the RF electrical power at the photodetector output to the RF electrical power which modulates the VCSEL. Therefore, it should be emphasized that the

associated 3 dB corner frequency $f_{3\,\mathrm{dB}}$ corresponds to an only 1.5 dB decay of the modulated optical signal. As a figure of merit, the modulation current efficiency factor (MCEF) specifies the increase of the 3 dB corner frequency with bias current I as [4]

$$\mathrm{MCEF} = \frac{f_{3\,\mathrm{dB}}}{\sqrt{I - I_{\mathrm{th}}}} \,, \tag{1}$$

where I_{th} is the threshold current.

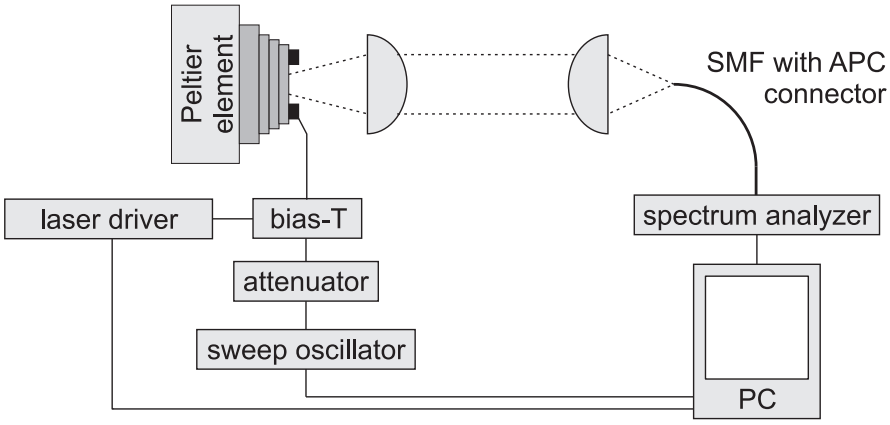

Fig. 2: Schematic drawing of the experimental setup for measurements of the small-signal modulation response.

Figure 2 illustrates the experimental setup employed to measure the small-signal modulation response. The VCSEL is driven by a constant current generated by a laser driver (ILX Lightwave, model LDC-3724B) and a low-power RF modulating signal generated by a sweep oscillator (Hewlett Packard, model HP83620A). The VCSEL chip is contacted via a coplanar microprobe (Cascade Microtech Inc., model ACP40-SG-200) with a signal–ground configuration. A bias-tee (Anritsu, model A3N1026) is used to combine the RF and DC current signals. An RF attenuator (Hewlett Packard, model HP8493C) attenuates the backward microwave reflections due to impedance mismatch between the VCSEL and the 50 Ω measurement system. The light is coupled into a single-mode fiber (SMF) and measured by a spectrum analyzer (Hewlett Packard, HP70000 system) through its internal RF photodetector[2]. To avoid unwanted optical feedback, both sides of the single-mode fiber are angle-polished[3]. Moreover anti-reflection-coated lenses are employed. Using a Peltier element, the temperature of the wafer holder can be increased up to 120 °C. All measurement instruments are controlled by a personal computer (PC) using the general purpose interface bus (GPIB). The small-signal modulation response curves of a VCSEL with 3 µm active diameter at different bias currents are depicted in Fig. 3 (left) for room-temperature operation. The frequency characteristics of all cables, bias-tees, attenuators, and the RF photodetector are numerically subtracted to obtain only the modulation response of the VCSEL.

[2]Lightwave section, HP70810B.

[3]Angled physical contact (APC) connector: The normal to the front surface of the optical fiber is tilted by 8 degrees with respect to the fiber axis.

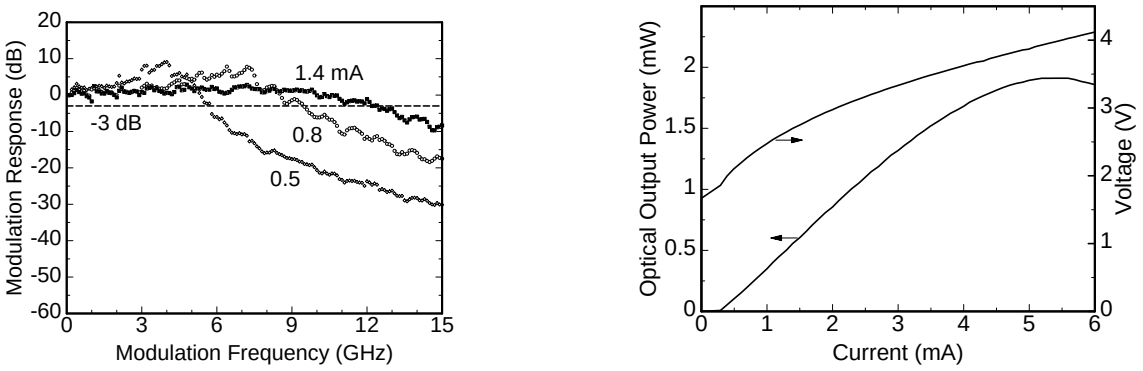

Fig. 3: Small-signal modulation response curves of a flip-chip-bondable VCSEL chip with 3 µm active diameter at different bias currents (left), and LIV characteristics of the same device (right). Both measurements were done at 20 °C ambient temperature.

A 3 dB bandwidth of 5.7 GHz is obtained at only 0.5 mA bias current. This bias is just 0.25 mA above threshold, see Fig. 3 (right). The maximum bandwidth is about 12 GHz, which well exceeds the 5 GHz specification for MAC-TFC. The modulation behavior at different bias currents was also measured at an elevated substrate temperature of 65 °C for the same VCSEL. Figure 4 depicts the extracted 3 dB corner frequencies versus $\sqrt{I - I_{\mathrm{th}}}$ at 20 and 65 °C ambient temperatures, where the MCEF values are as high as 12.3 and 10.6 GHz/$\sqrt{\mathrm{mA}}$, respectively.

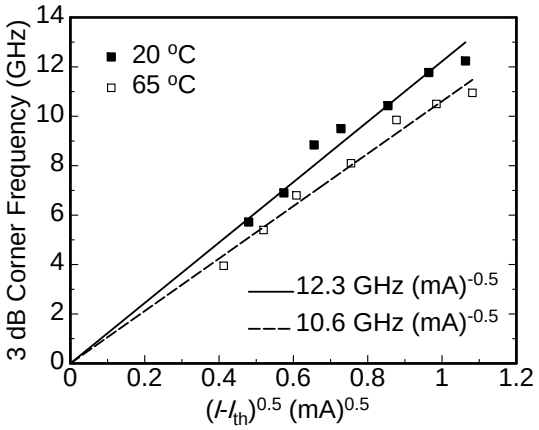

Fig. 4: 3 dB corner frequency in dependence of $\sqrt{I - I_{\mathrm{th}}}$ for the VCSEL from Fig. 3 at 20 and 65 °C ambient temperatures. The two lines are linear fits. Their slopes are given and represent the MCEFs.

3.2 Intrinsic modulation behavior

The modulation response curves introduced so far represent the superposition of the intrinsic frequency modulation response of the VCSEL and the modulation response of the electrical parasitics attributed to the structure of the VCSEL chip. The extrinsic

bandwidth limitation associated with the electrical parasitics can be represented by an electrical equivalent-circuit model. In order to obtain the intrinsic modulation characteristics of the VCSEL, two additional RF measurement techniques are applied in this work. The first method consists of measuring the microwave reflection curves, namely the S-parameter S_{11} from which the electrical parasitic elements of the equivalent-circuit model can be extracted and its bandwidth limitation be calculated [5]. The second technique is the measurement of the relative intensity noise (RIN) spectra [6]. It should be emphasized that each method allows to extract the intrinsic modulation behavior of the VCSEL. We have employed both techniques in order to improve the consistency of our results. In what follows we are presenting these two techniques in more details.

3.3 Microwave reflection spectrum

From a small-signal analysis of the laser rate equations, the modulation response introduced in the previous section can be approximated by the three-pole transfer function [4]

$$|M(f)|^2 = \frac{A f_\mathrm{r}^4}{(f_\mathrm{r}^2 - f^2)^2 + (\gamma f/(2\pi))^2} \cdot \frac{1}{1 + (f/f_\mathrm{p})^2} \,. \tag{2}$$

The first term represents the intrinsic carrier–photon interaction, which results in the ideal damping-limited modulation behavior of the semiconductor laser, where A is a device-dependent constant, f_r is the resonance frequency, and γ is the damping coefficient. The second term accounts for the parasitic elements found in the laser equivalent-circuit model, where f_p is its 3 dB corner frequency. A simple first-order low-pass is assumed. The approximation (2) does not account for the laser bandwidth limitation due to carrier transport, which seems not to be a speed-limiting effect for the frequency range up to 20 GHz. Figure 1 (right) depicts the physical origin of an equivalent-circuit model for the VCSEL impedance behavior, quite similar to the one proposed in [6]. The model takes into account the bondpad capacitance C_pad, the series resistance of the mirror R_m, the track inductance L, and the oxide aperture resistance R_a. C_a represents a combination of the capacitance of the active region and of the oxide layer. Above laser threshold, the active region is modeled as a short-circuit for small-signal conditions due to Fermi level pinning. At low frequencies, the VCSEL impedance is real and is given by the sum of R_m and R_a. As the frequency increases, C_a dominates over R_a, and the real part of the impedance reduces to R_m. From the input impedance

$$Z(f) = \left(\mathrm{i}2\pi f C_\mathrm{pad} + \left(\frac{R_\mathrm{a}}{1 + \mathrm{i}2\pi f C_\mathrm{a} R_\mathrm{a}} + R_\mathrm{m} + \mathrm{i}2\pi f L \right)^{-1} \right)^{-1} \tag{3}$$

of the equivalent circuit, one can obtain the reflection coefficient or scattering parameter

$$S_{11} = \frac{Z - Z_0}{Z + Z_0} \,, \tag{4}$$

where i is the imaginary unit and Z_0 is the impedance of the measurement system, which is usually 50 Ω. The microwave reflection spectra $S_{11}(f)$ of VCSEL chips are measured at

different bias currents using a 50 Ω network analyzer[4] in order to obtain the associated input impedance spectra $Z(f)$. By allowing the equivalent-circuit parameters to vary, the measured input impedance can be fit. For all curve fits in what follows, the Levenberg–Marquardt algorithm is applied.

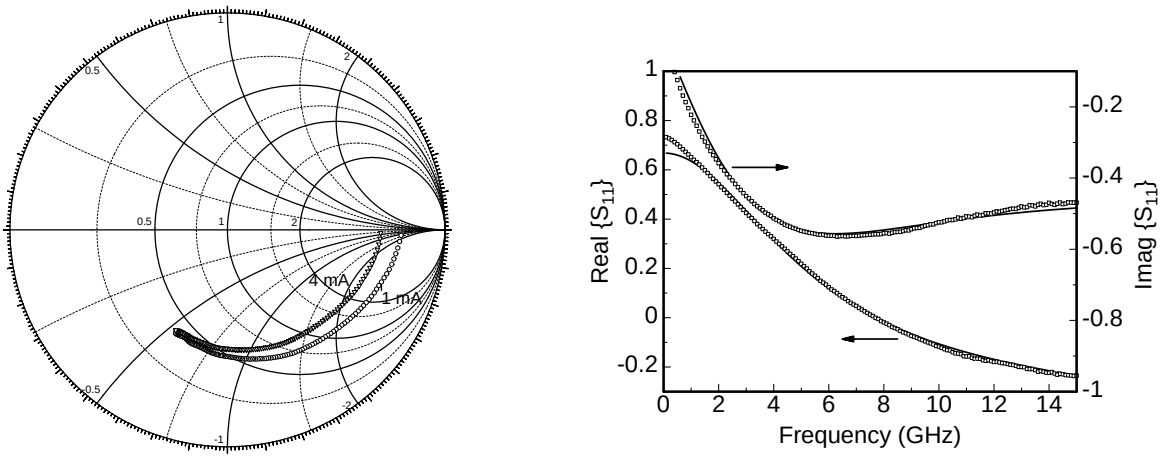

Fig. 5: Measured S_{11} spectra in a Smith chart of a VCSEL chip with 3.6 µm active diameter at 1 and 4 mA bias currents at room temperature (left). Real and imaginary parts of S_{11} of the same VCSEL at 3 mA drive current at room temperature (right). The solid lines (right) represent the modeled S_{11} using the equivalent-circuit model displayed in Fig. 1 (right) fit to the measurement data.

Figure 5 (left) depicts measured S_{11} data in a Smith chart over a frequency range from 0.1 to 15 GHz in 100 MHz steps at 1 and 4 mA bias currents. Figure 5 (right) illustrates the real and imaginary parts of the measured S_{11} spectrum for the same VCSEL chip at 3 mA bias current along with curve fits from the equivalent-circuit model. The resulting R_m, C_pad, and L are 47 Ω, 180 fF, and 70 pH, respectively. The extracted R_a and C_a values change with bias current and are listed in Table 1. In particular, R_a decreases

Table 1: Extracted values of the equivalent-circuit elements at different bias currents for the VCSEL chip from Fig. 5.

Bias current (mA)	1	2	3	4
R_a (Ω)	271	230	205	191
C_a (fF)	376	392	403	414

with increasing bias current, which is consistent with the decrease of the VCSEL differential resistance in the current–voltage curve at higher bias. We also observe that C_a increases with bias current. This bias-dependent behavior might be attributed to the diffusion capacitance C_d representing the transport of charge carriers through the active

[4]Spectrum analyzer HP8510C, S-parameter test-set HP8517A, and synthesized sweeper HP83651A.

region. C_d increases with increasing bias current [7]. Based on the extracted values of the equivalent-circuit elements, the electrical bandwidth can be determined from the 3 dB corner frequency f_p of the parasitic transfer function

$$M_\mathrm{p}(f) = \frac{V_{R_\mathrm{a}}}{V_\mathrm{s}} = \frac{\frac{A_3}{Z_0} \cdot \frac{A_2}{A_1+A_2+A_3}}{\left(1+\frac{A_2}{A_1}\right) \cdot \left(1+\frac{A_3}{Z_0} \cdot \frac{A_2}{A_1+A_2+A_3}\right) - 1} \tag{5}$$

with

$$A_1 = \frac{R_\mathrm{a}}{1 + \mathrm{i}2\pi f C_\mathrm{a} R_\mathrm{a}} \ , \tag{6}$$

$$A_2 = \mathrm{i}2\pi f L + R_\mathrm{m} \ , \tag{7}$$

and

$$A_3 = \frac{1}{\mathrm{i}2\pi f C_\mathrm{pad}} \ , \tag{8}$$

where V_s and V_{R_a} are the small-signal modulating voltages generated by the source and reaching the active region, respectively. Inserting the fit parameters, the 3 dB bandwidth of $|M_\mathrm{p}(f)|^2$ is approximately 5.2 GHz, showing a weak dependence on the bias current. Using (2) and the extracted f_p, precise fits of the measured modulation response curves can be performed, as evident from Fig. 6. Doing this, we have implicitly approximated $|M_\mathrm{p}(f)|^2$ from (5) by the first-order low-pass term in (2). The deviation is less than 0.15 dB up to a frequency of 15 GHz. Finally, the resonance frequency f_r and the damping coefficient γ can be extracted. The so-called K-factor is then obtained from the slope of the damping coefficient plotted against the square of the resonance frequency, as shown in Fig. 7. The theoretical damping-limited 3 dB bandwidth is then given as [4]

$$f_\mathrm{max} = \frac{\sqrt{8}\pi}{K} \ . \tag{9}$$

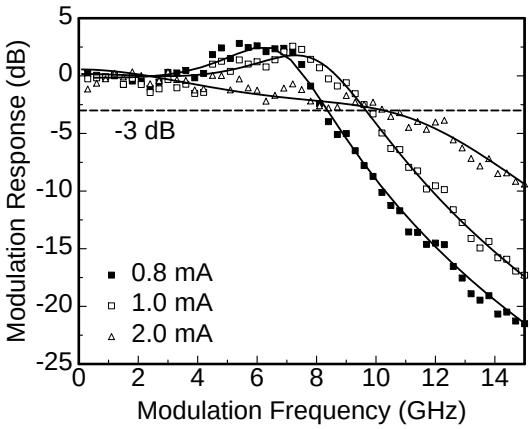

Fig. 6: Small-signal modulation response curves of a flip-chip-bondable VCSEL with 3.6 µm active diameter at different bias currents and room temperature. The solid lines are curve fits according to (2).

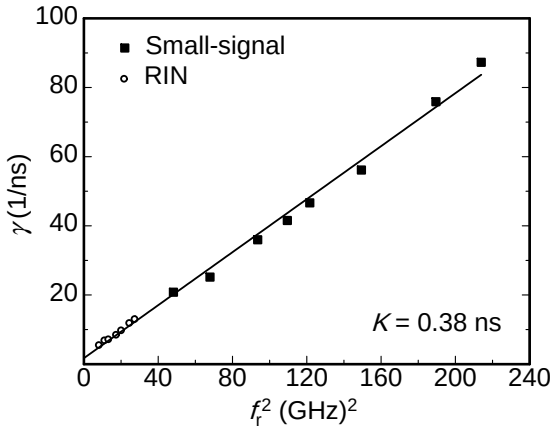

Fig. 7: Damping coefficient γ versus resonance frequency f_r squared of a VCSEL with 3.6 µm active diameter. Square symbols are the values obtained by curve fitting of measured small-signal modulation characteristics shown in Fig. 6, while circles are the values obtained by fitting the measured RIN spectra shown in Fig. 8 (right).

3.4 Relative intensity noise

Even with a noise-free VCSEL current driver, fluctuations will be present in a VCSEL's steady-state output power because of spontaneous emission. This noise characteristic is conveniently described by the RIN. More specifically, RIN relates the noise of the optical power $\delta P(t)$ to the mean power $\langle P \rangle$ as [8]

$$\mathrm{RIN} = \frac{\langle \delta P^2 \rangle}{\langle P \rangle^2} \ , \tag{10}$$

where the angular brackets denote an average over the observation time. Since the RIN is parasitics-free (note that the laser is driven by a CW signal), it can be employed not only to determine the noise characteristics of a laser, but also to examine its intrinsic modulation behavior. The RIN spectrum can be fit to extract f_r and γ using [4]

$$\mathrm{RIN}(f) = \frac{Cf^2 + D}{(f_\mathrm{r}^2 - f^2)^2 + (\gamma f/(2\pi))^2} \ , \tag{11}$$

where C and D are device-dependent constants. Figure 8 (left) shows the experimental setup employed to measure the RIN spectra. It is similar to the one used for small-signal modulation response measurements. A wide-band (10 GHz) low-noise amplifier (LNA, Miteq, model AMF-3D-001100-25-13P) is added after an external optical receiver (Picometrix, model AD-50xr). The optical receiver consists of an RF photodetector and a transimpedance amplifier with 20 dB gain. The noise spectrum is recorded using a microwave spectrum analyzer (Hewlett Packard, HP70000 system)[5]. The frequency characteristics of all cables, the bias-tee, the optical receiver, and the amplifier as well as the noise floor of the microwave spectrum analyzer and the shot noise of the RF photodiode

[5]The RF section HP70908A is employed.

are numerically subtracted to obtain the RIN of the VCSEL. The RIN spectra for different currents and fit curves using (11) are depicted in Fig. 8 (right) for a VCSEL that is nominally identical to the one from Fig. 6.

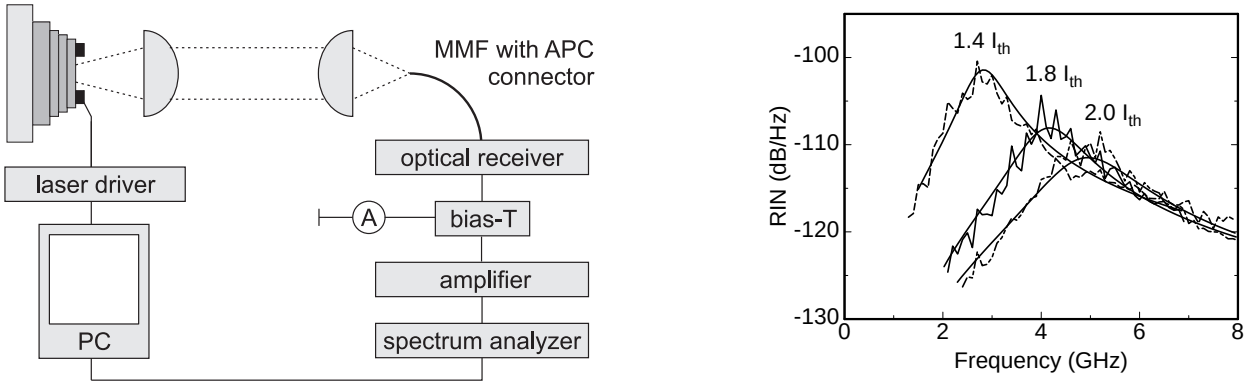

Fig. 8: Experimental setup used to measure RIN (left). RIN spectra of a VCSEL chip with 3.6 µm active diameter at different drive currents and room temperature (right). The solid lines are curve fits according to (11).

The resonance frequencies f_r and damping coefficients γ have been extracted and added to Fig. 7. The resultant K-factor is 0.38 ns and the maximum 3 dB bandwidth f_max is 23.4 GHz according to (9), with a high level of consistency between data points from the small-signal response and the RIN approach. The bandwidth of the VCSEL chips is thus limited by the electrical parasitics which have a 3 dB electrical bandwidth of only 5.2 GHz. The extraction procedure was more difficult from the RIN curves compared to the modulation response curves, especially for the damping coefficients which depend somewhat on the initial estimates. Moreover, the dynamic range of the RIN measurements is low due to the high noise floor originating mainly from the thermal noise of the optical receiver and to smaller extent from the thermal noise of the LNA. Shot noise plays a subordinate role. Therefore, increasing the dynamic range demands reducing the thermal noise and consequently smaller electrical bandwidths of the employed optical receiver and the LNA. The (f_r^2,γ) data points from RIN measurements in Fig. 7 are only in the low-frequency range due to the limited bandwidths of the employed LNA and the optical receiver (less than 10 GHz). For a reliable extraction of the data points, the resonance frequency should be about 3 to 4 GHz smaller than the system bandwidth, which limits the maximum extractable f_r to about 5 to 6 GHz.

4. Conclusion

We have reported the dynamic characterization of 894.6 nm VCSELs to be incorporated in Cs-based MEMS atomic clocks. The required modulation bandwidth of about 5 GHz is reached close above threshold. Maximum bandwidths above 10 GHz have been measured even at elevated temperatures up to 65 °C. For the investigation of the intrinsic modulation characteristics of the VCSELs, precise curve fitting procedures of measured RIN and

small-signal modulation spectra have been employed. A K-factor of less than 0.4 ns and a maximum 3 dB bandwidth exceeding 22 GHz are obtained.

5. Acknowledgments

The authors thank Y. Men for performing the electron beam lithography for grating fabrication. They wish to thank S. Renz, W. Schwarz, G. Liu, and T. Purtova, for their help in the processing and characterization. A very special thanks goes to Pierluigi Debernardi for the invention of the surface grating technique employed in this work and numerous simulations done in the past. Funding by the EC within its seventh framework programme (FP7) under grant agreement number 224132, project MAC-TFC is acknowledged.

References

[1] N. Cyr, M. Têtu, and M. Breton, "All-optical microwave frequency standard: a proposal", *IEEE Transactions on Instrumentation and Measurement*, vol. 42, no. 2, pp. 640–649, 1993.

[2] A. Al-Samaneh and D. Wahl, "Continuous-wave characteristics of MEMS atomic clock VCSELs", *Annual Report 2009, Institute of Optoelectronics, Ulm University*, pp. 41–46, 2009.

[3] R. Michalzik, J.M. Ostermann, and P. Debernardi, "Polarization-stable monolithic VCSELs", in *Vertical-Cavity Surface-Emitting Lasers XII*, C. Lei, J.K. Guenter (Eds.), Proc. SPIE 6908, pp. 69080A-1–16, 2008.

[4] R. Michalzik and K.J. Ebeling, "Operating Principles of VCSELs", Chap. 3 in *Vertical-Cavity Surface-Emitting Laser Devices*, H. Li and K. Iga (Eds.), pp. 53–98. Berlin, Germany: Springer-Verlag, 2003.

[5] R. Olshansky, P. Hill, V. Lanzisera, and W. Powazinik, "Frequency response of 1.3 μm InGaAsP high speed semiconductor lasers", *IEEE J. Quantum Electron.*, vol. QE-42, no. 9, pp. 1410–1418, 1987.

[6] D. Wiedenmann, R. King, C. Jung, R. Jäger, R. Michalzik, P. Schnitzer, M. Kicherer, and K.J. Ebeling, "Design and analysis of single-mode oxidized VCSEL's for high-speed optical interconnects", *IEEE J. Select. Topics Quantum Electron.*, vol. 5, no. 3, pp. 503–511, 1999.

[7] S.M. Sze, *Physics of Semiconductor Devices*, 2nd edition. New York, USA: John Wiley and Sons, 1981.

[8] K. Petermann, *Laser Diode Modulation and Noise*. Dordrecht, The Netherlands: Kluwer Academic Publishers, 1991.